Supporting Information

Impact of oxygen vacancy occupancy on charge carrier dynamics in $BiVO_4$ photoanodes

Shababa Selim,[1] Ernest Pastor,[1]* Miguel García-Tecedor,[2] Madeleine R. Morris,[1] Laia Francàs,[1] Michael Sachs,[1] Benjamin Moss,[1] Sacha Corby,[1] Camilo A. Mesa,[1] Sixto Gimenez,[2] Andreas Kafizas,[1,3] Artem A. Bakulin,[1] James R. Durrant[1]*

Corresponding authors: j.durrant@imperial.ac.uk; e.pastor11@imperial.ac.uk

[1]Department of Chemistry and Centre for Plastic Electronics, MSRH, White City Campus, Imperial College London, W12 0BZ
[2]Institute of Advanced Materials (INAM), Universitat Jaume I, 12006 Castelló, Spain
[3]The Grantham Institute, Imperial College London, South Kensington, London SW7 2AZ

Table of Contents

1. Materials fabrication

All materials were prepared on FTO substrate (2.5 cm x 2.5 cm, TEC 15, Hartford Glass Co.). Before deposition, the substrates were washed with a standard glass cleaner, followed with deionised water, acetone and iso-propanol and subsequently heated to 500 ^{o}C for 10 minutes. All chemicals were purchased from Sigma-Aldrich unless specified otherwise.

Dense, flat $BiVO_4$ photoanode films were prepared using a modified metal organic decomposition, previously reported.[1,2] The obtained films were monoclinic scheelite (Figure S1) and oxygen deficient (Figure S2). Bismuth nitrate pentahydrate (0.1455 g, 200 mM) was dissolved in acetic acid (1.5 mL, VWR) and vanadyl acetyl acetone (0.0768 g, 30 mM) was dissolved in acetyl acetone (10 mL, VWR). The two solutions were then mixed and stirred at room temperature for 30 minutes to prepare sol-gel. The sol-gel mixture was subsequently deposited by spin-coating. 50 µL of the solution was used per layer. Following the deposition of each layer, the substrates were calcined to 450 ^{o}C for 10 minutes. 14 layers were deposited, giving film thickness of approximately 350 nm. After the deposition of the final layer, the films were calcined at 450 ^{o}C for 5 hours, forming densely packed $BiVO_4$ thin films.

2. Characterisation

X-ray diffraction (XRD) XRD patterns were measured using a modified Bruker-Axs D8 diffractometer with parallel beam optics equipped with a PSD LinxEye silicon strip detector. The instrument uses a Cu source for X-ray generation (V = 40 kV, I = 30 mA) with Cu Kα1 (λ = 1.54056 Å) and Cu K α2 radiation (λ = 1.54439 Å) emitted with an intensity ratio of 2:1. The incident beam was kept at 1° and the angular range of the patterns collected between 10 ≤ 2θ° ≤ 66 with a step size of 0.05°.

X-ray photoemission spectroscopy (XPS) XPS data were obtained from a Thermo Scientific K-Alpha spectrometer equipped with an Al Kα X-ray source (1486.6 eV) coupled with an 180° double focussing hemispherical analyser with a 2S detector at an operating pressure of 1×10^{-8} mbar and a flood gun to minimise charging effects from photoemission. Films were mounted on to the sample holder adhered with carbon tape. All core lines were referenced against the C 1s (C-C), which is at 284.8 eV. Data were subsequently processed and analysed on the CASAXPS software package.

3. Experimental set-up

Experiments were carried out in a typical three-electrode cell equipped with a platinum mesh as counter electrode, Ag/AgCl (saturated KCl) as reference electrode and the $BiVO_4$ film as the working electrode, using an Autolab potentiostat (PGSTAT 101). A 0.1 M potassium phosphate buffer (pH 7) was used as the electrolyte in all experiments. Applied potentials measured *vs* Ag/AgCl ($V_{Ag/AgCl}$) were converted to applied potentials *vs* the reversible hydrogen electrode (V_{RHE}) using the Nernst equation:

$$V_{RHE} = V_{Ag/AgCl} + 0.0591 \times pH + V^0_{Ag/AgCl}$$

Where $V^0_{Ag/AgCl}$ is the standard potential of the Ag/AgCl reference electrode in saturated KCl (197 mV).

Photoelectrochemical measurements A 75 W Xe lamp fitted with a KG3 filter, with the light intensity adjusted to 1 sun was utilised as the illumination source. The scan rate used for linear sweep voltammetry was 10 mV s^{-1}. For the temperature dependence study on photoelectrochemical performance (Figure S7c), the measurements were conducted in a quartz cell fitted in a custom-made heating device. The heating device has been detailed previously in Morris *et al.*[3]. The sample and the counter electrode were placed inside the quartz cell. To avoid correcting the applied potential for temperature, the reference electrode was placed in a separate container that was connected to the electrolyte in the quartz cell using a salt-bridge. At each set temperature, the sample was allowed to equilibrate for 20 minutes before measurements were taken.

Impedance spectroscopy The impedance spectroscopy (EIS) measurements were carried out in a potentiostat/galvanostat Autolab (model PGSTAT-30). Measurements were performed in a three-electrode configuration, where a platinum wire was used as counter electrode, the sample under study was used as the working electrode, and an Ag/AgCl (3 M KCl) electrode was used as the reference electrode. An aqueous phosphate buffer solution at pH 7 (0.1 M NaH_2PO_4/Na_2HPO_4) was used as electrolyte. The electrochemical measurements were referred to the reversible hydrogen electrode (RHE) through the Nernst equation above, where $V^0_{Ag/AgCl}$ (3 M KCl) is 0.210 V. The exposed area of the sample to the electrolyte was 1 cm^2.

Spectroelectrochemical experiments Spectroelectrochemistry (SEC) measurements are presented as the difference in the optical absorption spectra as a function of applied potential ($\Delta O.D._V$), with respect to the open-circuit potential (V_{oc}), determined using:

$$\Delta O.D._V = O.D._V - O.D._{Voc}$$

The technique is detailed in Pastor *et al.*[4] Absorption spectra were taken using a Cary 60 UV-Vis spectrometer (Agilent Technologies), fitted with a spectroelectrochemical cell.

Thermal difference measurements Thermal difference measurements are presented as the difference in the optical absorption spectra as a function of applied temperature ($\Delta O.D._T$), with respect to the room temperature (T_0, 295 K) determined using:

$$\Delta O.D._T = O.D._T - O.D._{To}$$

Absorption spectra were taken using a Cary 60 UV-Vis spectrometer (Agilent Technologies), fitted with a temperature cell. The temperature of the sample was varied between 295K and 321 K using the heating device described above. At each set temperature, the sample was allowed to equilibrate for 20 mins before absorption measurements were taken. All measurements were taken in 0.1 M phosphate buffer, under open-circuit conditions.

Ultrafast transient absorption measurements Transient absorption measurements were conducted on the femtosecond to nanosecond timescale using a regeneratively amplified Ti:sapphire laser system (Solstice, Spectra-Physics) and Helios spectrometers (Ultrafast Systems), which generates 800 nm laser pulses (pulse width: 92 fs, repetition rate: 1 kHz). To generate the *pump*, a fraction of the 800 nm beam was directed through a sequence of optical parametric amplifier (TOPAS Prime, Spectra-Physics) and a frequency mixer (NirUVis, Light Conversion) to tune the excitation wavelength. The intensity of the *pump* was modulated using neutral density filters, and measured using an energy meter (VEGA, P/N 7Z01560, OPHIR Photonics), fitted with a 0.5 mm diameter aperture. The *pump* beam at the sample was slightly larger than 0.5 mm in diameter. A visible white light continuum (WLC) was used as the *probe*, generated from a fraction of the 800 nm pulse, focused onto a Ti:sapphire crystal. The *probe* beam is delayed with respect to the *pump* beam by a motorised delay stage, before the generation of the WLC. To reduce the noise, the WLC was split into two beams, where one is passed through the sample, and the other is used as reference. Both beams are subsequently focused onto separate fibre-optic coupled multichannel spectrometers (CMOS sensors). Alternate *pump* pulses were blocked using a synchronised chopper (500 Hz). As such, absorption spectra of the excited and unexcited sample were obtained to determine the time-resolved absorption difference spectrum. Time zero was then adjusted such that it occurs at the half-amplitude of the initial rise. The presented decay kinetics were averaged over a spectral range of ca. 5 nm.

Ultrafast pump-push-probe measurements These measurements were obtained using a modified TA set up described above. A fraction of the 800 nm beam was used to seed a β-barium borate (BBO) doubling crystal. BBO produced 400 nm light by second harmonic generation which was used as the ''*pump*''. To generate the *push,* fraction of the 800 nm beam was directed through a sequence of optical parametric amplifier (TOPAS Prime, Spectra-Physics) and a frequency mixer (NirUVis, Light Conversion) and tuned to 2060 nm. The intensities used were between the range 3 – 10 mJ cm^{-2}. The time delay between the *pump* and the *push* was adjusted and fixed at ~10 picosecond with a mechanical stage. The *probe* (a visible white light continuum) was generated from a fraction of the 800 nm pulse, focused onto a Ti:sapphire crystal. The output of the *pump* (modulated at 500 Hz), the broadband visible-near-infrared (~400 - 850 nm) *probe* and the *push* were focused onto a ~0.2 mm^2 spot on the sample. The same detection system used for TA measurements was employed in these experiments.

Transient absorption spectroscopy (microsecond - second) Transient absorption spectroscopy (TAS) measurements were carried out on a home-built configuration consisting of a Nd:YAG laser (OPOTEK Inc., Opolette 355 laser system, 7 ns pulse width) at 355 nm. The laser frequency was set to 0.7 Hz, and the laser intensity adjusted to 300 μJ cm^{-2}. The light source used for the probe beam is a 100 W Bentham IL1 tungsten lamp coupled to a monochromator (OBB-2001, Photon Technology International). To filter scattered laser light, the probe beam was directed through longpass filters and another monochromator (set to the same wavelength as the probe beam). To detect the transmitted photons, a Si-photodiode was utilised (Hamamatsu). The obtained data were processed through an amplifier (Costronics). The microsecond – millisecond data were recorded by an oscilloscope (Tektronics TDS 2012B), and the millisecond to second data were recorded with a DAQ card (National Instruments, NI USB-6211). For each transient absorption decay, the data were averaged over 100 laser pulses. The kinetic traces were subsequently smoothed using adjacent averaging (20) using a graphing software (Origin Labs). The system and data acquisition were controlled by a home programmed Labview software. For the bias dependence studies (Figure S6), measurements were conducted in a three-electrode cell and the potential was applied using an Autolab potentiostat (PGSTAT 101, Metrohm). Temperature dependence measurements (Figure 4c and S7b) were carried out in a quartz cell using the same heating device described above.

Transient photocurrent measurements (TPC) Transient photocurrent data were obtained with a modified TAS setup and using the same excitation source as TA measurements in a three-electrode photoelectrochemical cell. The laser frequency was set to 0.7 Hz, and the laser intensity adjusted to 300 μJ cm^{-2}. Potential was applied using a ministat (Sycopel Scientific Ltd.). The transient photocurrent signal was recorded by the oscilloscope coupled to the ministat. The system and data acquisition were also controlled by a home programmed Labview software. Charge extraction was subsequently determined by integrating the transient photocurrent trace. The bias dependence TPC measurements were carried out in a three-electrode cell (Figure S6). For the temperature dependence TPC studies (Figure 4a and S7a), the measurements were conducted in a quartz cell using the same heating device described above. The sample and the counter electrode were placed inside the quartz cell. To avoid correcting the applied potential for temperature, the reference electrode was placed in a separate container that was connected to the electrolyte in the quartz cell using a salt-bridge.

Determining the DOS representative from SPEC data The density of states (DOS) was determined from the difference spectra as a function of applied bias (relative to V_{oc}). Since a ΔO.D. corresponds to the change in the population of a given transition or state, by taking the derivative of ΔO.D. (465 nm) *vs* the applied potential, the states could be mapped from the spectral feature as function of bias.

4. Characterisation data (XRD, UV-Vis, XPS)

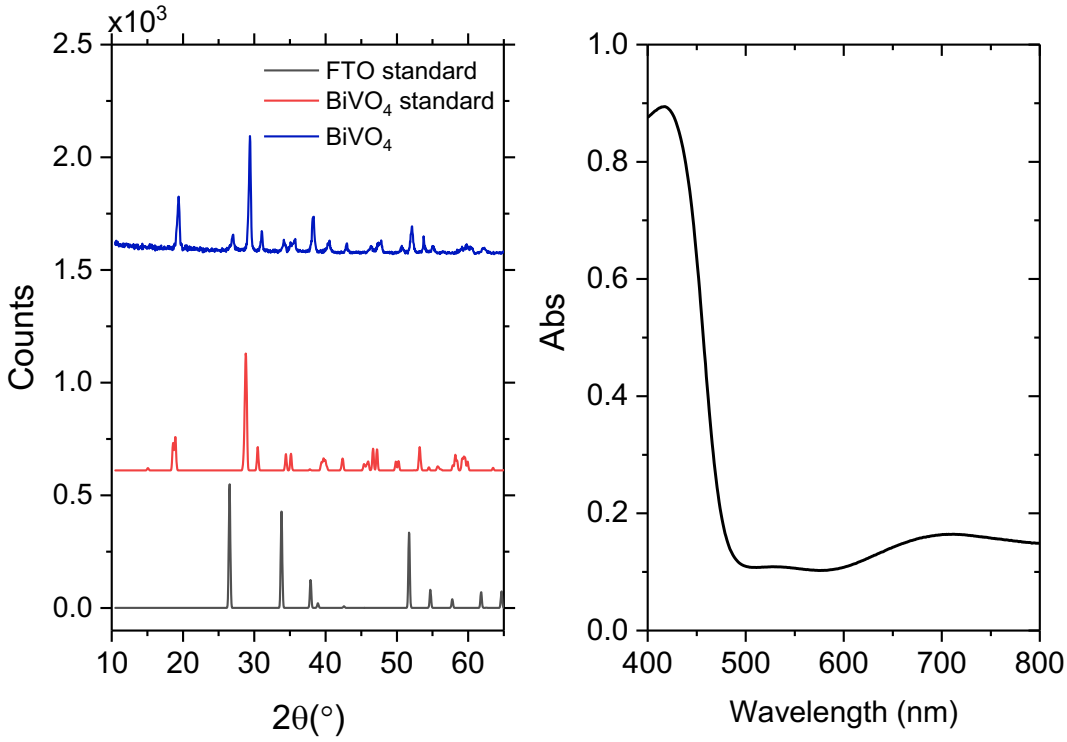

Figure S1| XRD and UV-Vis absorption spectra of $BiVO_4$ photoanodes. (a) Typical XRD patterns of $BiVO_4$ shown alongside reference standards (monoclinic scheelite $BiVO_4$ and tetragonal cassiterite F: SnO_2). (b) UV-Vis absorption spectrum.

a

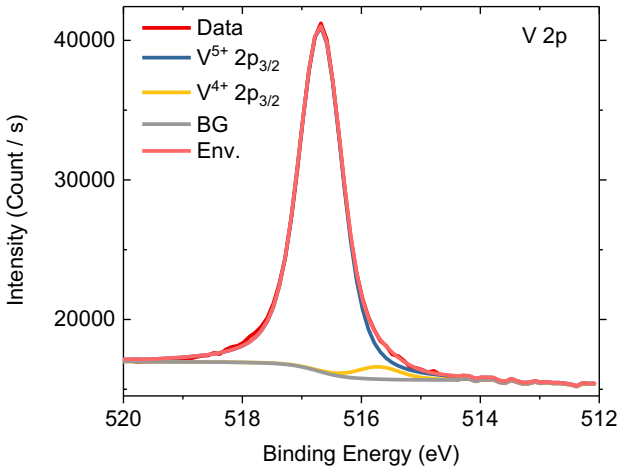

b

Peak	Area (V^{5+})	Area (V^{4+})	$\%V_o$
$2p_{3/2}$	26500	924	1.68%

Figure S2| XPS analysis. a, XPS scan of V($2p_{3/2}$) showing small proportion of V^{4+}. **b**, Determination of % oxygen vacancy (V_o) in $BiVO_4$ from the relative area of V^{4+} and V^{5+} from V($2p_{3/2}$) contributions. Since the excess electrons from each oxygen vacancy site gives rise to two equivalents of V^{4+} species, the surface $\%[V_o]$ is calculated using:

$$\%[Vo] = \left(\frac{Area_{V4+}}{Area_{V4+} + Area_{V5+}}\right) \times \frac{1}{2} \times 100\%.$$

5. Electrochemical and photoelectrochemical measurements

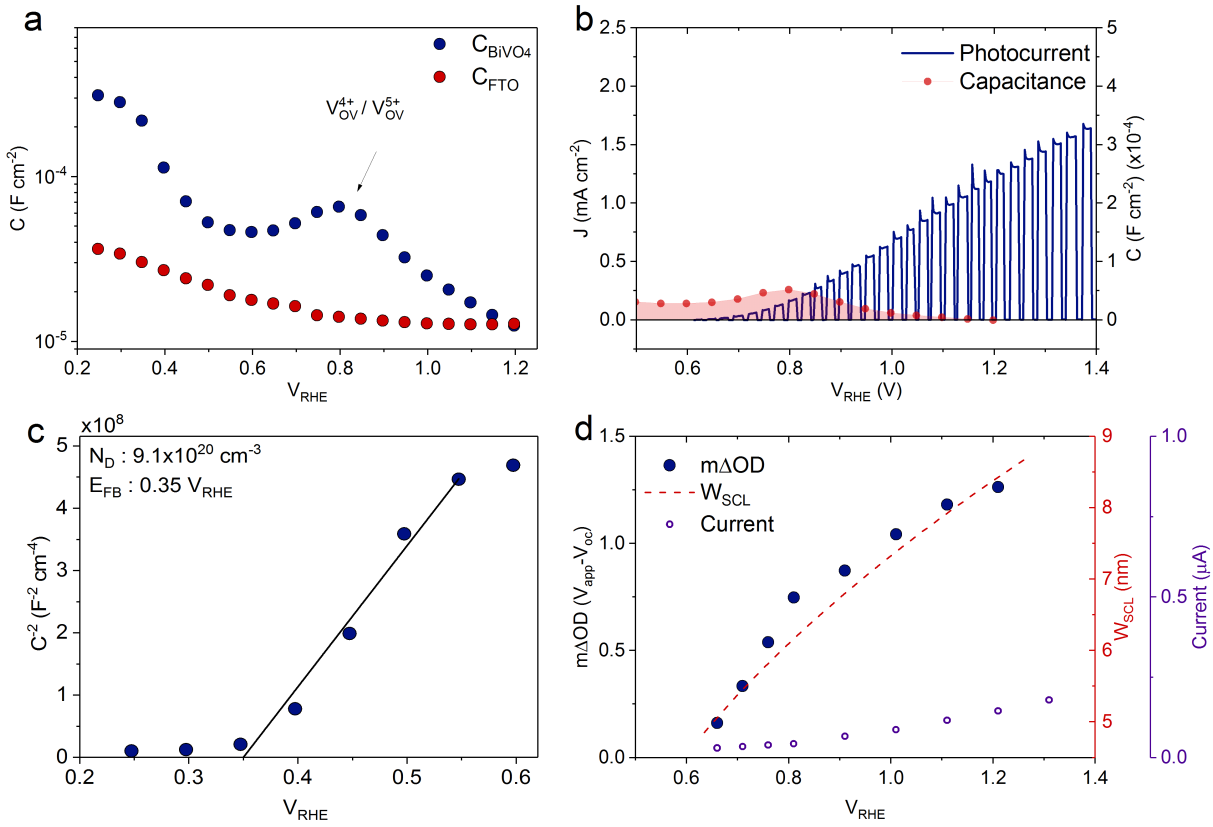

Figure S3| Relationship between the capacitance associated with $V_{OV}^{4+/5+}$, the photoelectrochemical response and the space charge layer formation in $BiVO_4$ photoanodes. a, The capacitance associated with V_{OV}^{5+}/V_{OV}^{4+} in $BiVO_4$ photoanode and the FTO substrate as a function of applied potential, in dark. **b**, The capacitance of the photoanode plotted against the photocurrent (under equivalent 1 sun illumination). The capacitance of the sub-band gap states coincides with the onset of photocurrent. **c**, The Mott-Schottky plot of the $BiVO_4$ photanode in 0.1 M potassium phosphate buffer, from which the donor density (N_D) and the flat-band potential (V_{FB}) were determined. The V_{FB} value determined for the photoanodes studied herein is more positive than previously reported for $BiVO_4$ (typically 0.1 – 0.3 V_{RHE}).[5,6] **d,** The optical signal observed in spectroelectrochemical measurements as a function of applied potential at 465 nm, relative to the V_{oc} (0.6 V_{RHE}), plotted against the space-charge layer width of the film. The space-charge layer width (W_{SCL}) is calculated using the equation: $W_{SCL} = \sqrt{\frac{2\varepsilon\varepsilon_0 (V-V_{FB})}{eN_D}}$, where ε and ε_0 are the relative permittivity of $BiVO_4$ (68),[7] and vacuum permittivity ($8.854 \times 10^{-12}\ F\ m^{-1}$), respectively; V is the applied potential; and e is the electronic charge ($1.602 \times 10^{-19}\ C$). The dark steady state current measured whilst applying the potential is also presented (purple open circles, right axis). All measurements were taken in 0.1 M phosphate buffer.

6. Electrochemical, thermal and transient absorption differential spectra

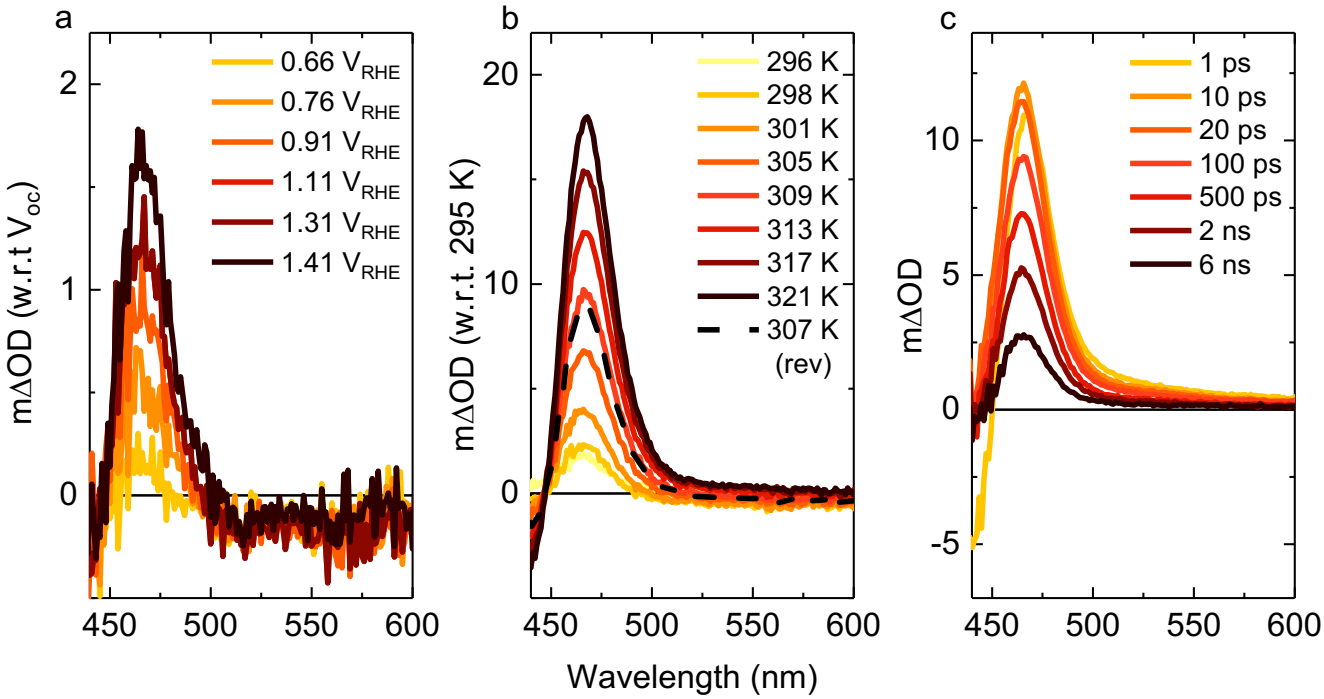

Figure S4| Difference spectra showing the optical absorption feature at 470 nm observed following the modulation of V_{OV} defect state electronic occupancy, in 0.1 M phosphate buffer (pH 7). a, Spectroelectrochemical difference spectra obtained under various applied electrical bias, plotted relative to the open circuit potential at 0.6 V_{RHE}. **b**, Thermally induced steady-state difference absorption spectra obtained under various applied temperatures under open circuit conditions, subtracted from 295 K, where the dotted line represents the spectrum obtained following cooling down to 307 K (rev) showing the reversibility (rev) of the process. **c**, Transient absorption spectra under open circuit conditions, illuminated from the electrolyte/electrode side with a 355 nm *pump* (300 μJ cm^{-2}).

7. Determination of the extinction coefficient of sub-bandgap states

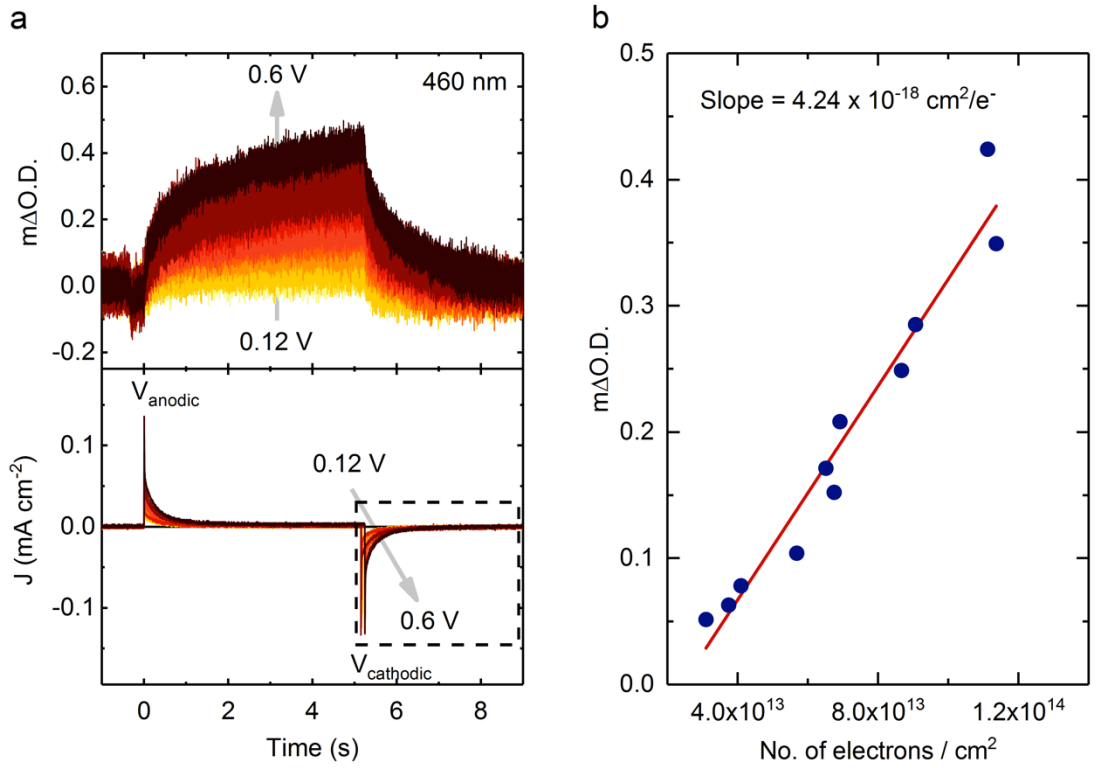

Figure S5| Determination of extinction coefficient of the sub-bandgap states associated with oxygen vacancies. A 5 second pulse of anodic potential in the range of 0.12 V - 0.6 V (*vs* Ag/AgCl) is applied to oxidise $[V_{OV}^{4+}]$ to $[V_{OV}^{5+}]$ which is followed by an 8 second pulse of cathodic potential (0.01 $V_{Ag/AgCl}$ (initial V_{oc})) to reduce the oxidised $[V_{OV}^{5+}]$ back to $[V_{OV}^{4+}]$. **a,** The optical signal corresponding to the change in the oxidation state of $[V_{OV}^{4+}]$ to $[V_{OV}^{5+}]$ probed at 460 nm (**top panel**) and the concomitant transient current signal associated with the oxidation of $[V_{OV}^{4+}]$ (positive spike) and reduction of $[V_{OV}^{5+}]$ (negative spike) (**bottom panel**). **b,** Plot of the optical signal ($[V_{OV}^{5+}]$) *vs* the number of electrons required to reduce $[V_{OV}^{5+}]$ to $[V_{OV}^{4+}]$, calculated by integrating the negative spike in the transient current. The measurements were conducted in the dark.

8. Comparison of electrochemical and thermal oxidation of $[V_{OV}^{4+}]$

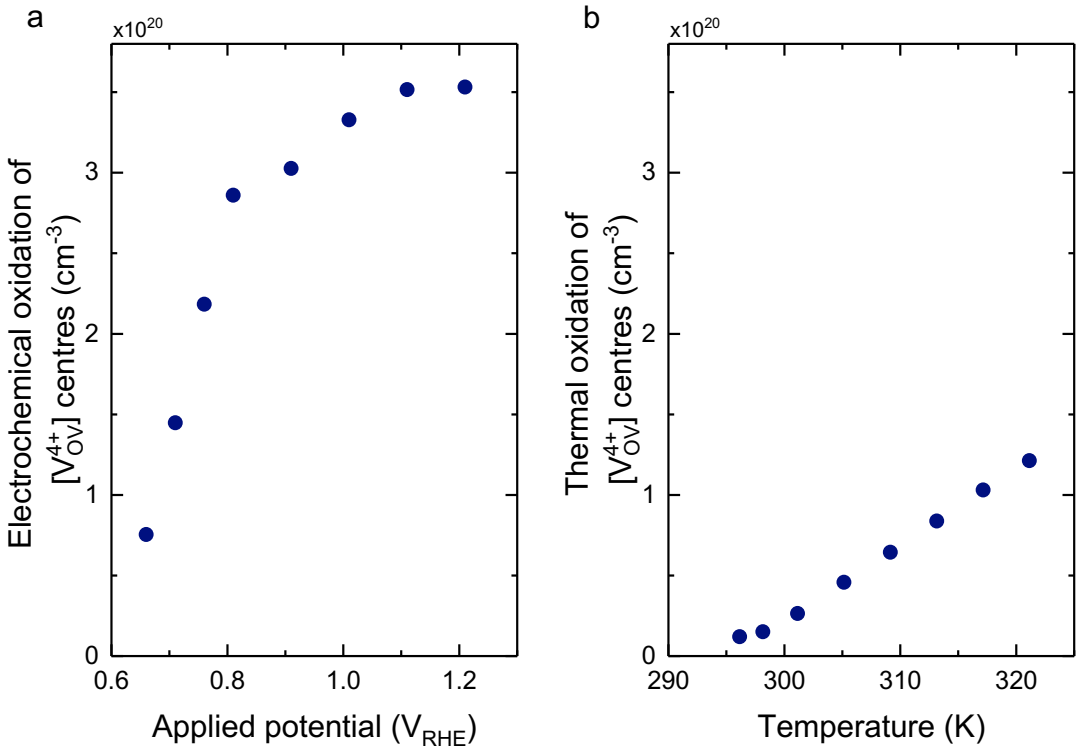

Figure S6| Comparison of the number of $[V_{OV}^{4+}]$ centres accessible electrochemically and thermally in $BiVO_4$ photoanodes. a, States accessible electrochemically within the space-charge layer width (W_{SCL}) as a function of applied potential. The W_{SCL} for a given potential is obtained as shown in **Figure S3d**. **b,** States accessible thermally across the thickness of the film as a function of temperature. The film thickness of the $BiVO_4$ photoanodes was 350 nm. The extinction coefficient value (4.24 $x10^{-18}$ cm^2/e^-) used to convert the optical signal in **Figure S4** (**a** and **b**) to the number of $[V_{OV}^{4+}]$ centres was determined in **Figure S5**. Whilst the number of $[V_{OV}^{4+}]$ centres accessible by applied potential saturates after 0.8 V_{RHE}, consistent with these states being associated with surface space charge layer formation, no such saturation is observed at elevated temperatures, within the temperature range studied herein signifying that thermal oxidation is a bulk process.

9. UV *Pump* - IR *Push* - Visible *Probe* spectra and kinetics

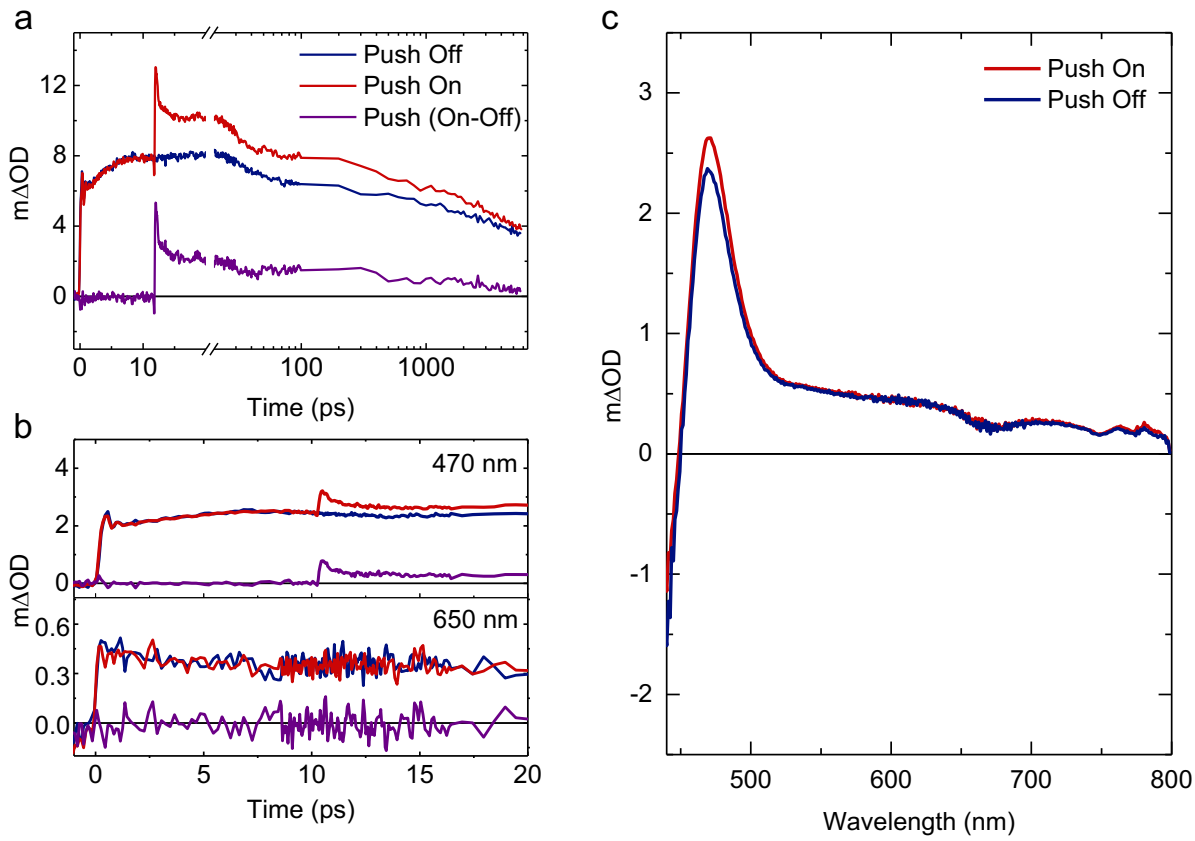

Figure S7| 3-pulse *pump-push-probe* measurements in air showing the effect of electron excitation from V_{OV}^{4+} to the conduction band, with λ_{ex}(*push*): 2060 nm. a, *Push* on and *push* off kinetics at 470 nm (femtosecond - nanosecond); *pump* and *push* excitation densities were 76 µJ cm^{-2} and 10 mJ cm^{-2}, respectively. **b,** Kinetics at 470 nm and 650 nm showing enhancement only at 470 nm band with the *push* excitation. **c,** *Push* On - Off spectra at a *push – probe* time delay of 15 picoseconds. The *pump* wavelength for all measurements were set to λ_{ex}(*pump*): 400 nm. For **b** and **c**, *pump* and *push* excitation densities were 200 µJ cm^{-2} and 3 mJ cm^{-2}, respectively. The difference in the absolute signal amplitudes arise from sample variations between independent measurements.

10. Transient absorption and transient photocurrent measurements

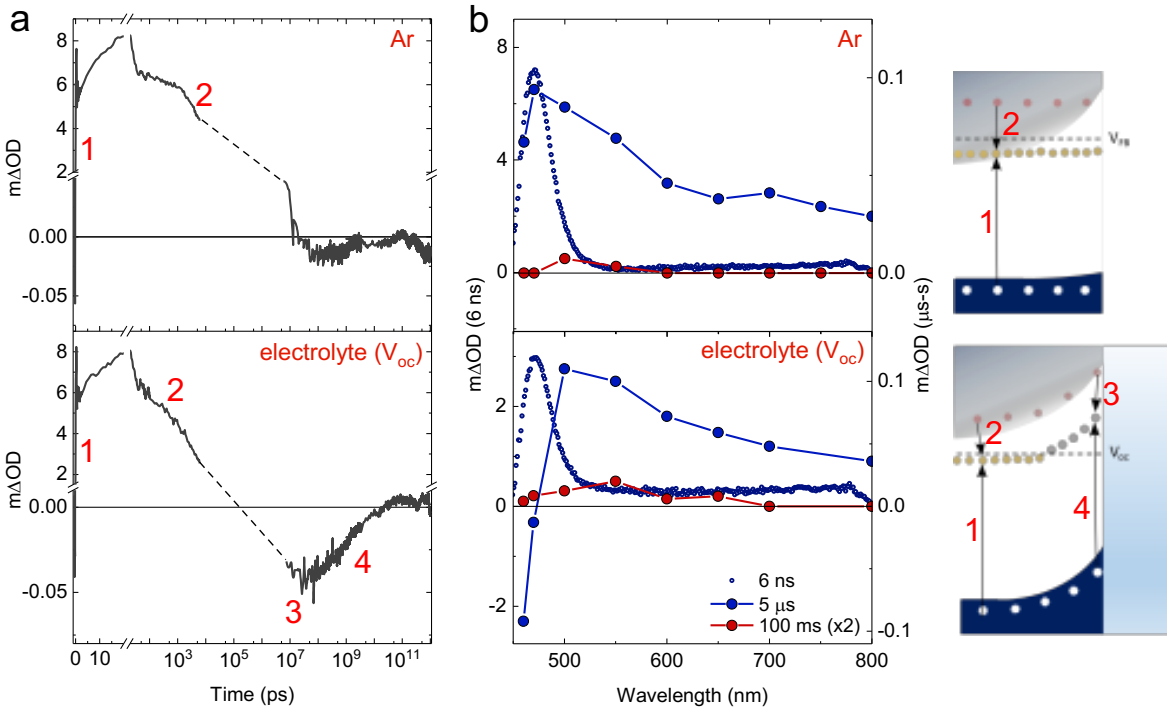

Figure S8| Effect of charge carrier trapping on charge carrier dynamics under inert atmosphere and in electrolyte. a, Transient absorption kinetics spanning from fs-ns timescale probed at 470 nm, to the µs-s timescale probed at 470 nm (dotted line is added to guide the eye) under inert atmosphere (top panel) and under open-circuit conditions (bottom panel). **b,** TAS spectra of $BiVO_4$ under inert atmosphere (Ar) (top panel) and under open circuit conditions (bottom panel) at 6 ns (purple), 5 µs (blue) and 100 ms (x2) (red); (excitation density: 300 µJ cm^{-2} (µs-s) and 250 µJ cm^{-2} (fs-ns) at 355 nm). The schematic adjacent to the panels illustrate the processes giving rise to the charge carrier dynamics where processes **(1)** and **(2)** outline bulk hole and electron trapping into Vov states. Process **(3)** shows electron trapping into oxidised V_{OV}^{5+} within the space charge layer, which subsequently recombine with surface holes (**4**).

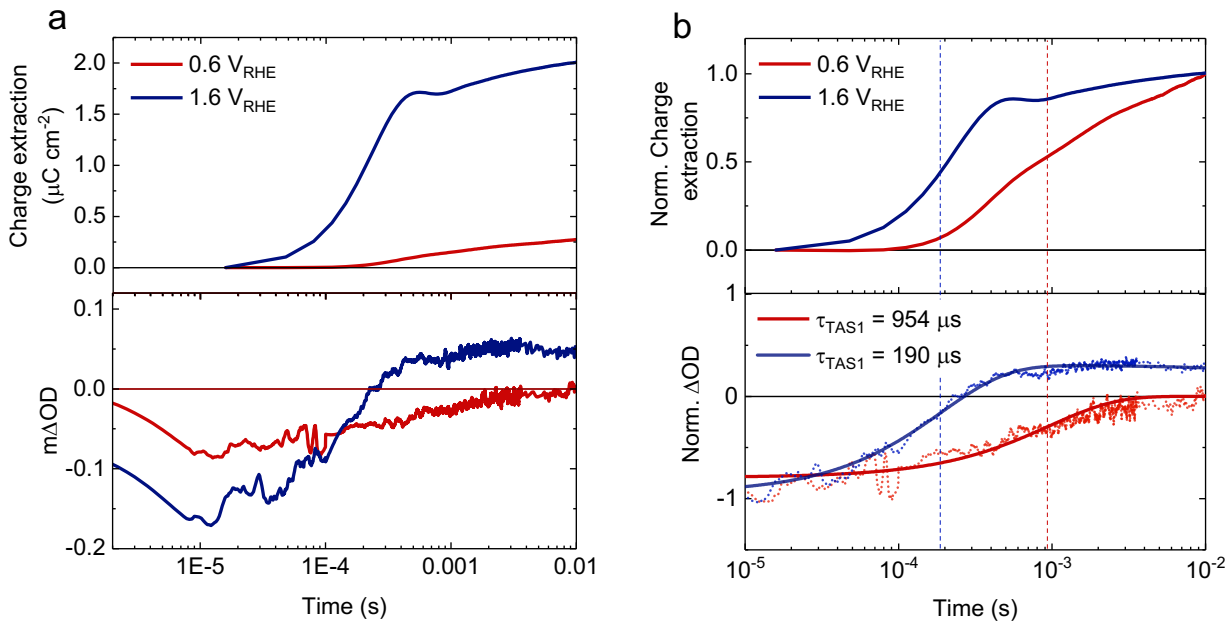

Figure S9| Electron trapping and electron extraction in $BiVO_4$ photoanodes under operational conditions. **a**, Transient charge extraction from $BiVO_4$ photoanode obtained with transient photocurrent measurements (top panel) with the concomitant transient absorption kinetics probed at 460 nm (bottom panel) showing the bleach in the signal due to electron trapping at 0.6 V_{RHE} and 1.6 V_{RHE}. Measurements were taken in 0.1 M phosphate buffer (pH 7) with λ_{ex}: 355 nm (300 μJ cm^{-2}). **b**, TPC and fitting of TA kinetics at 460 nm at 0.6 V_{RHE} (red) and 1.6 V_{RHE} (blue). TA kinetics were fitted using the exponential functions: $y = Ae^{-\frac{t}{\tau_{TAS1}}}$ and $y = Ae^{-\frac{t}{\tau_{TAS1}}} + Be^{-\frac{t}{\tau_{TAS2}}}$ for 0.6 V_{RHE} and 1.6 V_{RHE} respectively, where τ_{TAS1} represents time scale of charge extraction, and τ_{TAS2} represents decay of long-lived holes at the surface.

11. Temperature dependence studies

The activation energy of thermal trapping/de-trapping processes from TPC and TA measurements were calculated by determining the $t_{50\%}$ of charge extraction and TA signal decay as a function of temperature, respectively. The $t_{50\%}$ values were then used to calculate the activation energy using Arrhenius analysis, using the equation:

$$\ln\left(\frac{1}{t_{50\%}}\right) = \ln(A) - \frac{Ea}{R}\left(\frac{1}{T}\right)$$

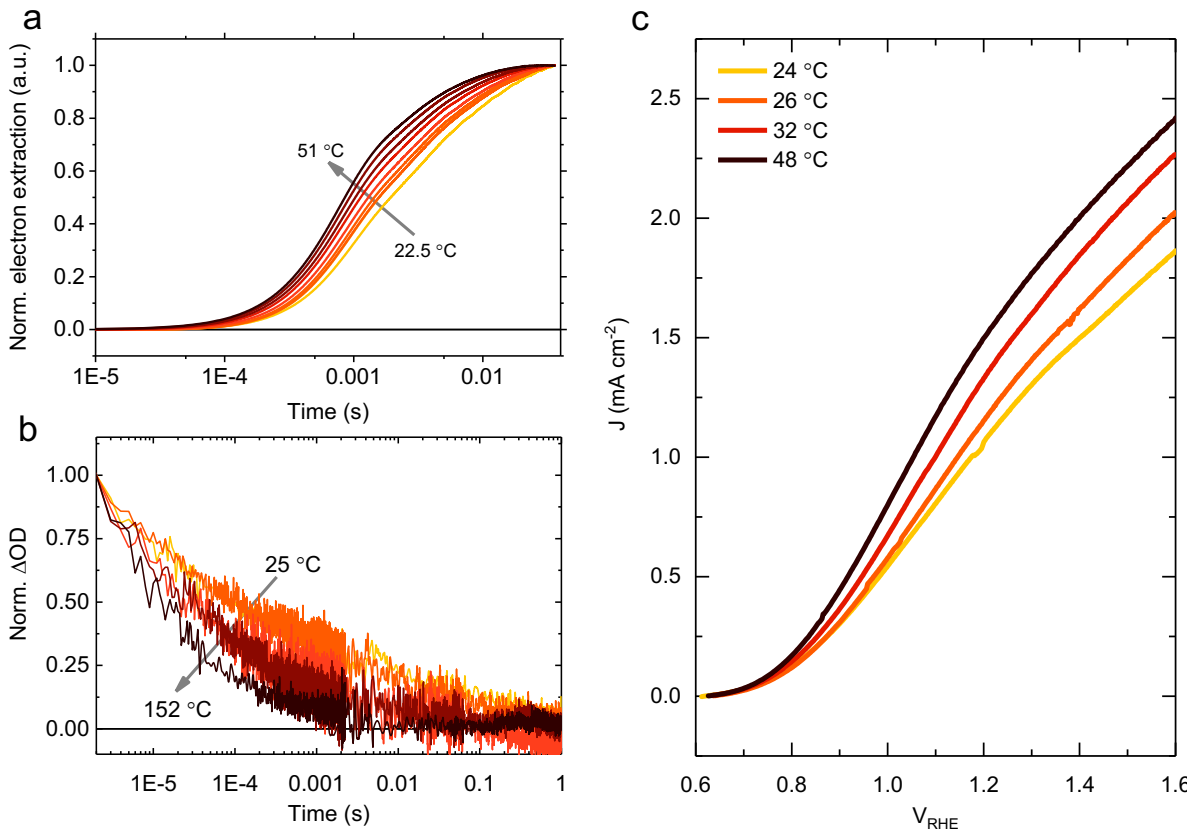

Figure S10| Temperature dependence studies of charge extraction, charge carrier dynamics and photoelectrochemical performance. a, Normalised TPC of $BiVO_4$ at 0.6 V_{RHE} with varying temperatures showing accelerated electron extraction with increasing temperature. **b**, Normalised TA kinetics of $BiVO_4$ probing valence band holes at 550 nm under inert atmosphere, showing faster charge recombination as a function of temperature. **c**, Photoelectrochemical performance of $BiVO_4$ photoanode under equivalent 1 sun illumination showing the increase in photocurrent at higher temperatures. It is noted that the film used for the TPC study does have a more cathodic photocurrent onset compared to the one used for linear sweep voltammetry. This is attributed to variations in $BiVO_4$ films.

12. Self-trapping *vs* trapping at defects (*i.e.* oxygen vacancies)

Distinguishing between a self-trapped carrier (small and large) or a carrier trapped in the 'vicinity' of a defect is not trivial (as they both give rise to a vanadium oxidation state of +4), especially as the presence of defects might itself influence the dynamics of polaron formation. Experimentally we find that the 470 nm optical signal tracks the concentration of redox states which was previously associated with oxygen vacancies by impedance spectroscopy (reference 39 in main paper). For the case of a self-trapped electron at a vanadium centre (formation of a polaron), this localisation may induce a stabilised electronic state below the conduction band. However, upon electrochemical oxidation of the electrode (oxidising the V^{4+}), we would imagine that the stabilised electronic state is unlikely to be present. On the contrary, when we are performing electrochemical oxidation (in the dark), using spectroelectrochemistry (Figure 2a in the main paper and Figure S4a), we observe the oxidised V^{5+} state and we can map the density of these states below the conduction band (Figure 1c in main paper) which correlates with the capacitance associated with the V_{OV}^{5+}/V_{OV}^{4+} redox couple. Based on this and complementary data, we conclude that this optical signal is a probe of phenomena directly linked to oxygen vacancies. Although, we do acknowledge that electrons trapped at defect sites may also incur lattice stabilisation therefore, our data by itself, does not rule out polaron formation, while further computational studies and experimental measurements such x-ray and time-resolved Raman might be necessary to unwind the link between defects and polaronic states.

References

1 Y. Ma, S. R. Pendlebury, A. Reynal, F. Le Formal and J. R. Durrant, *Chem. Sci.*, 2014, **5**, 2964–2973.

2 S. Selim, L. Francàs, M. García-Tecedor, S. Corby, C. Blackman, S. Gimenez, J. R. Durrant and A. Kafizas, *Chem. Sci.*, , DOI:10.1039/C8SC04679D.

3 M. R. Morris, S. R. Pendlebury, J. Hong, S. Dunn and J. R. Durrant, *Adv. Mater.*, 2016, **28**, 7123–7128.

4 E. Pastor, F. Le Formal, M. T. Mayer, S. D. Tilley, L. Francàs, C. A. Mesa, M. Grätzel and J. R. Durrant, *Nat. Commun.*, 2017, **8**, 14280.

5 A. J. E. E. Rettie, H. C. Lee, L. G. Marshall, J.-F. Lin, C. Capan, J. Lindemuth, J. S. McCloy, J. Zhou, A. J. Bard and C. B. Mullins, *J. Am. Chem. Soc.*, 2013, **135**, 11389–11396.

6 S. Wang, P. Chen, Y. Bai, J. H. Yun, G. Liu and L. Wang, *Adv. Mater.*, 2018, **30**, 1–7.

7 M. Valant and D. Suvorov, *J. Am. Ceram. Soc.*, 2004, **83**, 2721–2729.